



Article

Stability Assessment of p-i-n Perovskite Photovoltaic Mini-Modules Utilizing Different Top Metal Electrodes

Janardan Dagar ^{1,2,*}, Gopinath Paramasivam ^{1,2}, Carola Klimm ^{1,2}, Markus Fenske ^{2,3}, Christof Schultz ³, Rutger Schlatmann ^{3,4}, Bert Stegemann ³ and Eva Unger ^{1,2,5}

- ¹ HySPRINT Innovation Lab, Helmholtz-Zentrum Berlin, Kekuléstrasse 5, 12489 Berlin, Germany; gopinath.paramasivam@helmholtz-berlin.de (G.P.); klimm@helmholtz-berlin.de (C.K.); eva.unger@helmholtz-berlin.de (E.U.)
 - ² Young Investigator Group Hybrid Materials Formation and Scaling Kekuléstrasse 5, 12489 Berlin, Germany; markus.fenske@helmholtz-berlin.de
 - ³ School of Engineering—Energy and Information, HTW Berlin—University of Applied Sciences, Wilhelminenhofstr. 75a, 12459 Berlin, Germany; christof.schultz@helmholtz-berlin.de (C.S.); rutger.schlatmann@HTW-Berlin.de (R.S.); Bert.Stegemann@HTW-Berlin.de (B.S.)
 - ⁴ PVcomB/Helmholtz-Zentrum Berlin für Materialien und Energie GmbH, Schwarzschildstr. 3, 12489 Berlin, Germany
 - ⁵ Department of Chemistry & NanoLund, Lund University, Naturvetarvägen 14, 22362 Lund, Sweden
- * Correspondence: Janardan.Dagar@helmholtz-berlin.de



Citation: Dagar, J.; Paramasivam, G.; Klimm, C.; Fenske, M.; Schultz, C.; Schlatmann, R.; Stegemann, B.; Unger, E. Stability Assessment of p-i-n Perovskite Photovoltaic Mini-Modules Utilizing Different Top Metal Electrodes. *Micromachines* **2021**, *12*, 423. <https://doi.org/10.3390/mi12040423>

Academic Editor: Francesco Di Giacomo

Received: 25 March 2021
Accepted: 9 April 2021
Published: 13 April 2021

Publisher's Note: MDPI stays neutral with regard to jurisdictional claims in published maps and institutional affiliations.



Copyright: © 2021 by the authors. Licensee MDPI, Basel, Switzerland. This article is an open access article distributed under the terms and conditions of the Creative Commons Attribution (CC BY) license (<https://creativecommons.org/licenses/by/4.0/>).

Abstract: Long-term stability is one of the major challenges for p-i-n type perovskite solar modules (PSMs). Here, we demonstrate the fabrication of fully laser-patterned series interconnected p-i-n perovskite mini-modules, in which either single Cu or Ag layers are compared with Cu/Au metal-bilayer top electrodes. According to the scanning electron microscopy measurements, we found that Cu or Ag top electrodes often exhibit flaking of the metal upon P3 (top contact removal) laser patterning. For Cu/Au bilayer top electrodes, metal flaking may cause intermittent short-circuits between interconnected sub-cells during operation, resulting in fluctuations in the maximum power point (MPP). Here, we demonstrate Cu/Au metal-bilayer-based PSMs with an efficiency of 18.9% on an active area of 2.2 cm² under continuous 1-sun illumination. This work highlights the importance of optimizing the top-contact composition to tackle the operational stability of mini-modules, and could help to improve the feasibility of large-area module deployment for the commercialization of perovskite photovoltaics.

Keywords: self-assembled monolayer; module; electrode; perovskite; maximum power point; flakes; stability

1. Introduction

Metal-halide perovskite solar cells (PSCs) have attracted attention by demonstrating a small-area power conversion efficiency (PCE) of more than 25% in the last few years [1–8]. For large-scale utilization, solar module fabrication needs to be developed with a number of interconnected cells, compared to a small-area single cell [9,10]. Series-interconnected monolithic perovskite solar modules (PSMs) can be fabricated using P1–P2–P3 patterning steps [2,11,12], as in any other thin-film solar technology like CdTe or CIGS. The deposition and patterning steps are as follows. Initially, subcells are defined by patterning the ITO bottom electrode with a P1 scribe, then all active layers of the solar cell are deposited, and are then separated from each other by the P2 patterning step [9,13]. Subsequently, the metal back electrode is deposited and a final, P3 scribe separates the metal top contacts of the sub-cells. The principles of laser patterning of thin film have been widely discussed in fabrication of modules [14–16]. In p-i-n PSMs, p and n are hole and electron transport layers, and “i” refers to the perovskite layer [2]. As a preference, p-i-n PSMs can be fabricated using easy and low-temperature processing steps. In addition, this includes less absorptive contact layers

and shows low current density–voltage hysteresis [17]. However, several challenges have been addressed in the processing of highly efficient and stable p-i-n, such as poor wettability of the hole transport layer, upscaling of the perovskite layer and long-term stability of the perovskite modules [18,19]. In our previous work, we have extensively studied both picosecond and nanosecond laser pulses as used for P2 [9] and P3 [16] patterning steps to fabricate the mini-modules. We optimized the shorter picosecond laser pulses to remove the PbI_2 debris, generated during P2 and P3 patterning, and improved the performance of the perovskite mini-module [9,16].

With regard to the P3 patterning step, it has been reported that flaking, or the formation of large metal flakes or particles of top metal electrode, causes problems with the electrical isolation of the series interconnected sub-cells in modules [20]. The flaking causes fluctuations in the maximum power point (MPP) tracking under continuous 1-sun illumination, which result in a reduction in module performance and long-term stability due to intermittent lack of contact with the sub-cells [21]. To decrease the possibility of flaking of the metal electrode, several strategies have been applied, such as optimization of nanosecond or picosecond laser pulse, and wider P3 scribing with multiple time overlapping [16]. In addition, laser patterning with N_2 gas flow is used to remove the metal particles [21]. However, these solutions have been found difficult to employ for Cu and Ag metal top electrodes. Rather than being blasted away during the laser-ablation process, the metal seems to locally melt or rupture, creating metal flakes that point upward from the laser-scribe but remain physically connected to the metal back electrode. Consequently, it is highly important to resolve the issue of flaking back/top electrodes to make highly efficient and stable perovskite solar mini-modules.

In this study, we demonstrate a solution to this issue by using a bilayer metal electrode, via depositing a thin 30 nm-thick layer of additional gold (Au) on top of the 70 nm-thick copper (Cu) electrode by thermal evaporation [22,23]. The PSMs of three series interconnected cells with a Cu/Au bilayer top electrode exhibited an improved steady-state efficiency of 18.9% after continuous 11 h 1-sun illumination. In addition to the single-metal electrode, some alloyed or composite metal electrodes have also been investigated previously, in perovskite solar cells such as AgAl (silver–aluminum) [24] and NiAu (nickel–gold) [25]. However, the introduction of double metal layers (CuAu) has not been used to fabricate the p-i-n perovskite mini-module, because of the concern of long-term stability assessment. The PSMs with a Cu/Au electrode nullified the fluctuations which occurred in the MPP due to the formation of Cu metal particles at different interconnections of the cells. This module strategy enables the development of a highly efficient and stable large-area module.

2. Results and Discussion

In this work, perovskite solar mini-modules with a p-i-n configuration of Glass | ITO | 2PACz | $\text{Cs}_{0.15}\text{FA}_{0.85}\text{PbI}_{2.55}\text{Br}_{0.45}$ | C_{60} | SnO_2 | Cu | Au were fabricated as shown in Figure 1a. A detailed explanation of the PSM fabrication process is given in the experimental section. In short, PSMs were built on conductive indium tin oxide (ITO) substrates, prepared by P1 patterning. At first, high-quality hole-selective contacts with a self-assembled monolayer (SAM) of (2-(9H-carbazol-9-yl) ethyl) phosphonic acid (2PACz) were spin-coated on glass/ITO substrates. As a photoabsorber, CsFA ($\text{Cs}_{0.15}\text{FA}_{0.85}\text{PbI}_{2.55}\text{Br}_{0.45}$) was deposited over the 2PACz layer. Next, a layer of 23 nm of C_{60} was thermally deposited over the perovskite layer, which is further followed by ALD (Atomic Layer Deposition), which deposited a 20 nm SnO_2 layer, and the P2 patterning step was performed. Here we introduced three different top metal electrodes, such as Ag, Cu, and Cu covered with Au (Cu/Au) via thermal evaporation, and P3 patterning was performed to cut the metal electrode and connect subcells in series interconnection. Figure 1b showed the current flow in interconnected subcells to the mini-module. The layout of the 2.20 cm^2 module has been also shown in Figure 1c. The geometrical fill factor was calculated to be 91%. The aperture area used during characterization of the mini-module was 2.35 cm^2 , resulting in

an aperture efficiency of 16.60%. The non-active area of 0.15 cm² includes area losses due to the P1–P2–P3 interconnection.

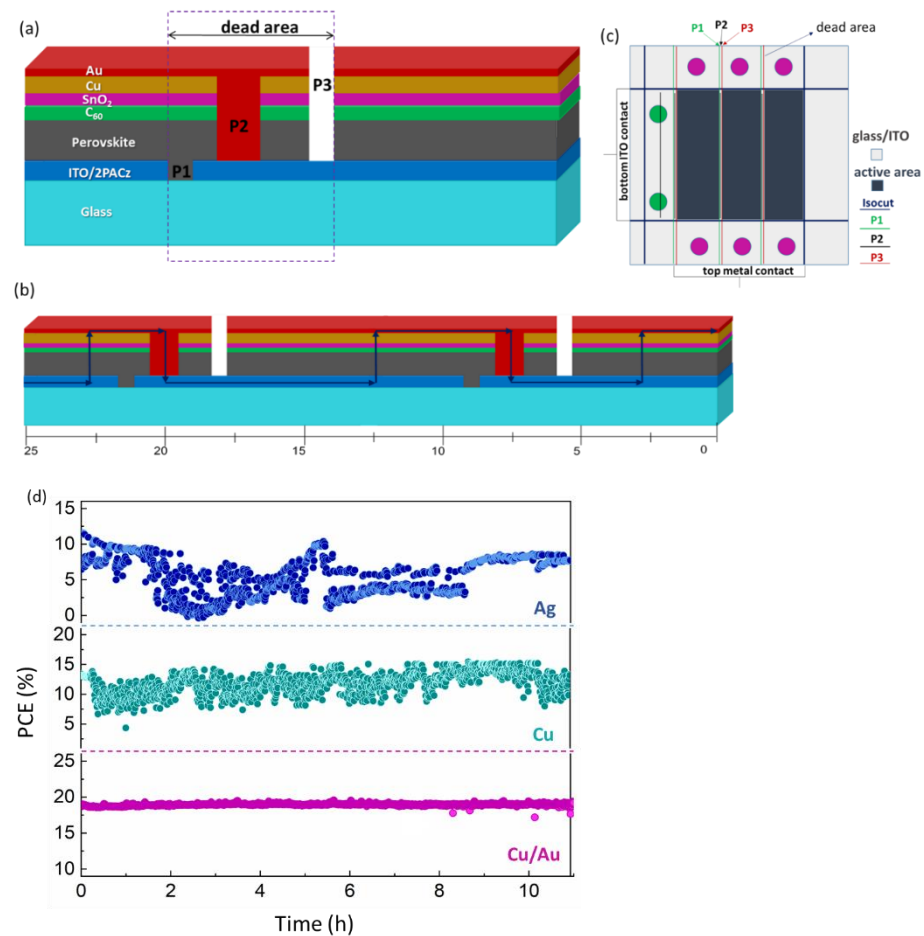


Figure 1. (a) The schematic device layout of p-i-n perovskite solar mini-modules with P1, P2 and P3 interconnections; (b) charge flow in the series connection among cells in a module; (c) layout of a 2.20 cm² module; and (d) long-term maximum power point tracking (MPPT) of p-i-n type perovskite solar modules (PSMs) with different metal top electrodes, such as Ag, Cu and Cu/Au, while measured under simulated 1-sun illumination.

Figure 1d shows the steady-state maximum power point efficiencies for the best-performing modules of each type over more than 11 h under continuous 1-sun illumination at 25 °C. Interestingly, we found that the long-term efficiency for Cu-based PSMs fluctuates with time, which further results in a complete breakdown of the PCE of the modules. The fluctuation in PCE is due to the fluctuation of steady-state current (I_{MPP}), while the steady-state voltage (V_{MPP}) was stable over time, as shown in Figures S1 and S2. Similar fluctuations in steady-state efficiency were also observed with a Ag electrode-based PSM, but were comparatively higher than those of a Cu-based PSM. In this study, we modified metal top-electrodes by depositing an additional 30 nm-thick gold (Au) layer on top of the 70 nm thick copper (Cu) electrode (Cu/Au), which improved the photovoltaic performance and removed the fluctuations in steady-state efficiency of the PSMs, as shown in Figures S1 and S2.

The current-voltage (I - V) curves of the best-performing 2PACz-based PSMs fabricated using different top electrodes are shown in Figure S3. The photovoltaic (PV) parameters of PSMs, such as short circuit current (I_{SC}), open-circuit voltage (V_{OC}), fill factor (FF), power conversion efficiency (PCE) obtained from IV curves, and power conversion efficiency at maximum power point (PCE_{MPP}) are summarized in Table 1. The PSMs with a Cu electrode exhibited superior performance compared to Ag-based PSMs. In particular, a

Cu/Au-based PSM yields a remarkable efficiency of 18.3%, as shown in Table 1. I - V curves of PSMs were also measured under dark conditions, as shown in Figure S4. We observed that PSMs with Cu/Au showed a low leakage of current compared to those with Ag- and Cu-based PSMs. We have also calculated the ideality factors for all PSMs with different top electrodes from their dark I - V curves, showing that Cu/Au exhibits a lower ideality factor of 0.288 compared to the Cu-based PSM 1.02 (as shown in Figure S5). This demonstrates that Cu/Au PSMs lead to better charge extraction, and thus higher FF values. As shown in Figure S6, MPPs have also been measured for a short time, showing a maximum PCE of 18.9% compared to Ag- and Cu-based PSMs.

Table 1. Summarized photovoltaic (PV) parameters of perovskite solar mini-modules with different metal top electrodes such as Ag, Cu and Cu/Au, while measured under simulated 1-sun illumination.

PV Parameters	Ag	Cu	Cu/Au
I_{SC} (mA)	16.27	15.93	15.83
V_{OC} (V)	3.36	3.39	3.40
FF (%)	68.3	71.7	74.1
PCE (%)	17.0	17.6	18.3
PCE_{MPP} (%)	16.9	17.3	18.9

Figure 2 shows the cross-section scanning electron microscopy (SEM) images ((Figure 2a–c) tilted by 10°) of PSMs, based on Figure 2a,d for Ag, Figure 2b,e for Cu and Figure 2c,f for Cu/Au top electrodes. We observed that Ag and Cu metal top electrode-based PSMs display Ag and Cu flakes (conductive metal particles), respectively, at the interconnection of the cells of modules. The isolation of the P1 or P3 scribe line caused redeposition of conducting particles after removal, as shown in Figure 2a,b,d,e. These flakes are responsible for the steady-state efficiency fluctuation, which further results in cell exclusion from the module circuit while stressing the module for a long period under 1-sun illumination at 25 °C. Optical microscopy images of the P2 and P3 patterning of the perovskite mini-module are also shown in Figure S7 with different electrodes. The formation of these conductive particles can be avoided by using an extra layer (30 nm) of gold (Au) over the copper (Cu) (70 nm) metal electrode (Cu/Au) [21]. Gold has the capability to bind strongly to the bottom layer and thus protects the Cu layer from forming the flakes, due to its high degree of thermal expansion [26,27]. EDX images of P3 scribing of both Cu- and Cu/Au-based PSMs are shown in Figure S8.

The most reliable metric to compare the module stability to the integrated lifetime energy yield (LEY) is calculated using the following equation [28,29]:

$$LEY = \int_0^t PCE(t) dt$$

where “ t ” refers to time. Figure 3 shows the LEY calculations for PSMs with different electrodes. The LEY for Cu/Au-based metal contacts showed that these modules had the highest figures, compared to the LEY produced by only Cu- and Ag-based perovskite mini-modules. This indicates that the modules showing the higher LEY values lead them to become more relevant for testing according to international standards such as the International Electrotechnical Commission (IEC) 61215 standard [30,31].

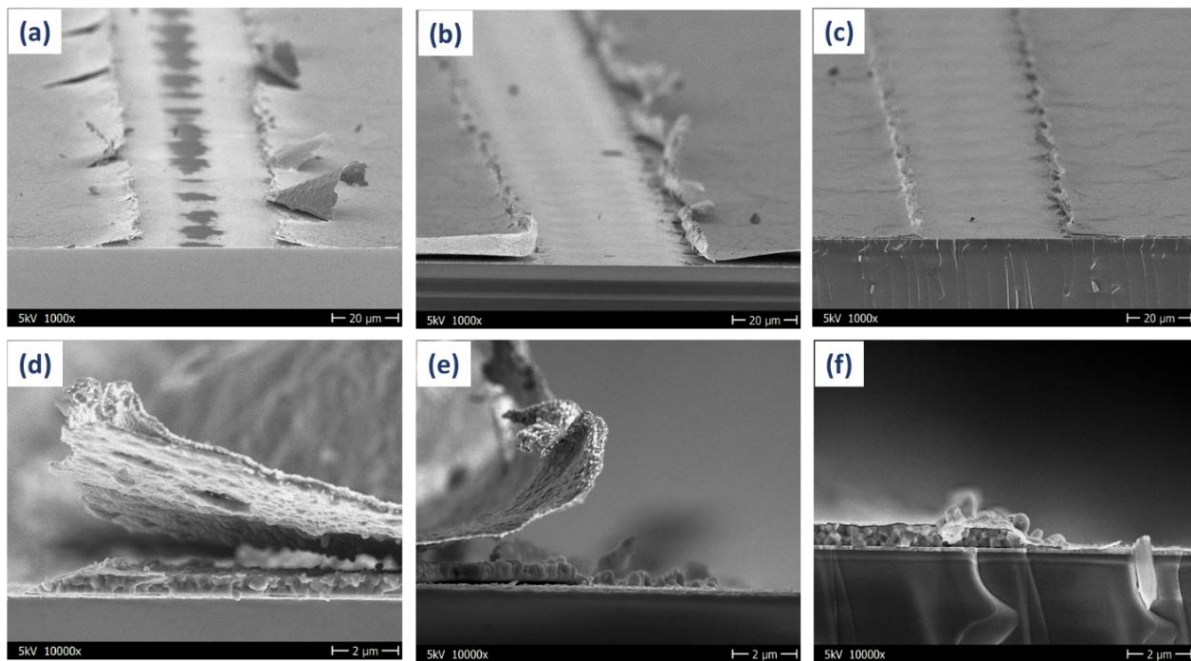


Figure 2. Scanning electron microscopic images of P2 and P3 patterning of (a,d) Ag electrode, (b,e) Cu electrode and (c,f) Cu/Au electrode of a perovskite mini-module.

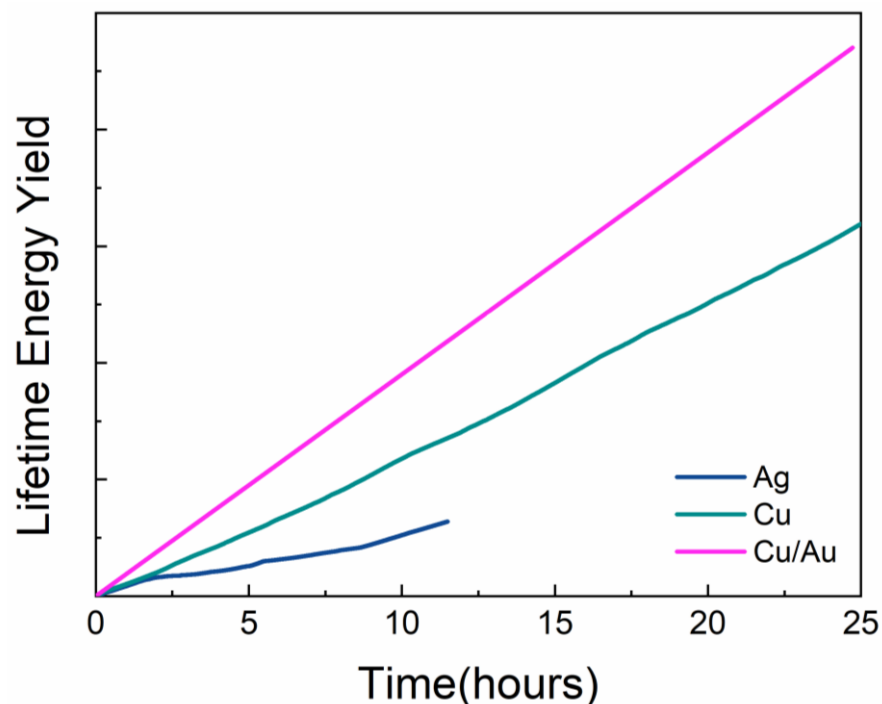


Figure 3. Integrated lifetime energy yield (LEY) of perovskite solar mini-module (PSM) with different top electrodes (Ag, Cu and Cu/Au).

3. Conclusions

In summary, fully laser-patterned monolithic p-i-n perovskite solar mini-modules have been fabricated comparing different metal electrodes as back contacts, namely, Cu, Ag or Cu/Au bilayers. We find that using Cu or Ag only leads to metal-back contact delamination and flaking upon P3-laser scribing, while the Cu/Au bilayer exhibits a very clean cut with good adhesion remaining between the device and metal contact. The perovskite modules with a Cu/Au bilayer top electrode therefore outperform devices with

Ag or Cu metal contacts, exhibiting close to 19% steady-state efficiency with negligible loss >11 h under continuous simulated AM1.5G illumination in an inert atmosphere.

4. Experimental Section

4.1. Materials

SAM (2PACz), lead (II) iodide (99.99% trace metals basis), and lead bromide (PbBr_2) were purchased from Tokyo Chemical Industry (TCI). Formamidinium iodide (FAI) and Cesium iodide (CsI) were obtained from Dynamo GmbH (Dresden, Germany) and abcr GmbH (Karlsruhe, Germany). Ethanol (anhydrous) was achieved from VWR Chemicals. Anisole, DMF, and DMSO chemicals were purchased from Sigma-Aldrich (St. Louis, MO, USA). All the chemicals were used as supplied without any further purification.

4.2. Perovskite Precursor Inks Preparation

The 1.2 M concentration of $\text{Cs}_{0.15}\text{FA}_{0.85}\text{PbI}_{2.55}\text{Br}_{0.45}$ perovskite ink was prepared using the following procedure. Initially, PbI_2 (446.4 mg), PbBr_2 (121.6 mg), FAI (185.5 mg), and CsI (57.4 mg) powders were scaled and mixed in vials, and dissolved with 0.750 mL of DMF and 0.250 mL of DMSO. The vial is kept on a shaker at 60 °C for 2 h. The resulting perovskite ink was filtered using a 0.2 μm -sized polytetra-fluorethylene (PTFE) filter.

4.3. Perovskite Mini-Module Fabrication

We fabricated a perovskite mini-module with an inverted (p-i-n) planar structure, with a layer configuration of $\text{ITO}|\text{2PACz}|\text{Cs}_{0.15}\text{FA}_{0.85}\text{PbI}_{2.55}\text{Br}_{0.45}|\text{C}_{60}|\text{SnO}_2|\text{CuAu}$, or Ag or Cu, using the following procedure. The perovskite mini-module fabrication is achieved by laser scribing of different layers using a Rofin-Baasel laser-patterning tool, see [9] for more details. In the P1 scribing process, indium tin oxide (ITO) glass substrates (of 25 mm \times 25 mm, resistivity of 15 $\Omega \text{ sq}^{-1}$) were subjected to a 1064 nm, picosecond (ps) laser (500 kHz, POD2, fluence of 7.33 J/cm^2 , speed of 400 mm/s) to cut the ITO electrode [9,16]. The patterned ITO substrates were cleaned sequentially according to the same procedure as described previously [2]. After that all substrates were transferred in a N_2 -filled glove box, where 1.2 mmol/L of 2PACz (MW = 275.24) solution was deposited on cleaned ITO substrate via spin-coating at a speed of 3000 rpm for 30 s. The substrates were immediately kept on a hotplate at 100 °C for 10 min. The CsFA perovskite layer was deposited on ITO/SAM substrates via spin-coating, with a spin speed of 3500 rpm with 5 s acceleration until 35 s steady duration. Anisole was used as an antisolvent. When 10 s were remaining to finish the spin coating, 250 μL of anti-solvent was dropped on the wetted perovskite layer. Next, the substrates were transferred to a hotplate at 100 °C for 30 min in a N_2 atmosphere.

All the substrates were transferred in the evaporation chamber, where C_{60} (23 nm) was thermally evaporated on top of the perovskite layer, at a rate of 0.05–0.12 $\text{Å}/\text{s}$ with a base pressure of 1×10^{-6} mbar. Next, 20 nm of a SnO_2 layer was deposited using an atomic layer deposition (ALD) technique, using an Arradiance GEMStar reactor. For the 20 nm deposition of the SnO_2 layer, 140 cycles were applied at an 80 °C substrate temperature. The layer stack of $\text{ITO}|\text{2PACz}|\text{Cs}_{0.15}\text{FA}_{0.85}\text{PbI}_{2.55}\text{Br}_{0.45}|\text{C}_{60}|\text{SnO}_2$ was patterned through a 532 nm ps laser (10 ps, pulsed at 100 kHz, POD5 and speed 200 mm/s, a fluence of $\sim 1.49 \text{ J}/\text{cm}^2$ with 3 passes) which is referred to as P2 scribing. For the top electrodes, Cu or Ag electrodes of 100 nm thickness were thermally deposited. For Cu/Au electrode deposition, at first, 70 nm of Cu was deposited, and immediately after, 30 nm gold was evaporated over the Cu in a metal evaporator at a base pressure of 1×10^{-6} mbar. P3 patterning was carried out to cut different top metal electrodes, to connect 3 cells in series using a ps laser at 532 nm (100 kHz, POD5, speed of 500 mm/s, three times scribing, each time with a fluence of 3.04 J/cm^2). The active area for a single cell is calculated to be 0.734 cm^2 , and for the module, 2.2 cm^2 , which is determined by microscopic imaging.

4.4. Sample Characterization

Solar Mini-Module Characterization

Current density–voltage (J – V) measurements of PSMs were performed, under AM 1.5 G 1000 Wm^{-2} under STC conditions using a sun simulator of AAA class calibrated with a silicon reference cell (Fraunhofer ISE, Freiburg, Germany), according to the same procedure as described previously [2].

4.5. SEM Measurements

SEM images were captured from a Hitachi S-4100 at 5 kV acceleration voltage system using a Zeiss Merlin.

Supplementary Materials: The following are available online at <https://www.mdpi.com/article/10.3390/mi12040423/s1>, Figure S1: Steady state voltage (V_{MPP}) measured under 1 sun illumination for both Cu and Cu/Au based mini modules, Figure S2: Steady state current (I_{MPP}) measured under 1 sun illumination for both Cu and Cu/Au based mini modules, Figure S3: Current–voltage (I – V) measurements of best-performing perovskite solar mini-modules (ITO|2PACz|CsFAPb(Br, I)₃|C₆₀|SnO₂|Ag or Cu or Cu/Au measured under simulated AM 1.5G illumination, Figure S4: Current–voltage (I – V)–characteristics perovskite solar mini-modules measured under dark, Figure S5: Ideality factors calculated from I – V curves measured under dark conditions for both Cu and Cu/Au based PSMs, Figure S6: The maximum power point tracking (MPPT) measured for 100 s at the fixed voltage near the maximum power point (MPP) derived from I – V measurements, Figure S7: Optical microscopy images of P2 and P3 patterning of perovskite mini-module. (a–c) PSMs with Cu electrode, (d–f) with Cu/Au electrodes, Figure S8: EDX images of P3 scribing of both Cu and Cu/Au based PSMs.

Author Contributions: J.D. was the main contributor to the idea and experimental part of this work. He fabricated and characterized the solar modules, analyzed the data, prepared the first draft of the manuscript and figures. G.P. supported fabricating the modules. M.F. and C.S. supported in laser patterning of the mini-modules. C.K. performed SEM and EDX measurements. R.S. and B.S. contributed to the scientific content through scientific discussions. E.U. supervised the project and contributed to the writing, as well as revisions of this manuscript. All authors have read and agreed to the published version of the manuscript.

Funding: This research received no external funding.

Acknowledgments: J.D. and E.U. acknowledge funding from the German Ministry of Education and Research (BMBF) for the Young Investigator Group Hybrid Materials Formation and Scaling (HyPerFORME) within the program “NanoMatFutur” (grant no. 03XP0091) and the “SNaPSHoTs” project (grant no. 01IO1806). The authors would like to acknowledge that lab infrastructure in the Helmholtz Innovation Lab was supported by the Helmholtz Energy Materials Foundry (HEMF) and the PEROSEED (ZT-0024) project, as well as the support of allocation of synchrotron radiation beamtime mySpot, BESSY II, HZB.

Conflicts of Interest: The authors declare no conflict of interest.

References

1. Best Research-Cell Efficiency Chart. 2021. Available online: <https://www.nrel.gov/pv/cell-efficiency.html> (accessed on 11 April 2021).
2. Dagar, J.; Fenske, M.; Al-Ashouri, A.; Schultz, C.; Li, B.; Köbler, H.; Munir, R.; Parmasivam, G.; Li, J.; Levine, I.; et al. Compositional and Interfacial Engineering Yield High-Performance and Stable p-i-n Perovskite Solar Cells and Mini-Modules. *ACS Appl. Mater. Interfaces* **2021**, *13*, 13022–13033. [[CrossRef](#)]
3. Bi, D.; Yi, C.; Luo, J.; Décoppet, J.-D.; Zhang, F.; Zakeeruddin, S.M.; Li, X.; Hagfeldt, A.; Grätzel, M. Polymer-templated nucleation and crystal growth of perovskite films for solar cells with efficiency greater than 21%. *Nat. Energy* **2016**, *1*, 16142. [[CrossRef](#)]
4. Saliba, M.; Matsui, T.; Domanski, K.; Seo, J.-Y.; Ummadisingu, A.; Zakeeruddin, S.M.; Correa-Baena, J.-P.; Tress, W.R.; Abate, A.; Hagfeldt, A.; et al. Incorporation of rubidium cations into perovskite solar cells improves photovoltaic performance. *Science* **2016**, *354*, 206–209. [[CrossRef](#)] [[PubMed](#)]
5. Stolterfoht, M.; Wolff, C.M.; Márquez, J.A.; Zhang, S.; Hages, C.J.; Rothhardt, D.; Albrecht, S.; Burn, P.L.; Meredith, P.; Unold, T.; et al. Visualization and suppression of interfacial recombination for high-efficiency large-area pin perovskite solar cells. *Nat. Energy* **2018**, *3*, 847–854. [[CrossRef](#)]

6. Wang, Z.; Lin, Q.; Chmiel, F.P.; Sakai, N.; Herz, L.M.; Snaith, H.J. Efficient ambient-air-stable solar cells with 2D–3D heterostructured butylammonium-caesium-formamidinium lead halide perovskites. *Nat. Energy* **2017**, *2*, 17135. [[CrossRef](#)]
7. Dagar, J.; Castro-Hermosa, S.; Lucarelli, G.; Cacialli, F.; Brown, T.M. Highly efficient perovskite solar cells for light harvesting under indoor illumination via solution processed SnO₂/MgO composite electron transport layers. *Nano Energy* **2018**, *49*, 290–299. [[CrossRef](#)]
8. Dagar, J.; Hirselandt, K.; Merdasa, A.; Czudek, A.; Munir, R.; Zu, F.; Koch, N.; Dittrich, T.; Unger, E.L. Alkali Salts as Interface Modifiers in n-i-p Hybrid Perovskite Solar Cells. *Sol. RRL* **2019**, *3*, 1900088. [[CrossRef](#)]
9. Schultz, C.; Fenske, M.; Dagar, J.; Zeiser, A.; Bartelt, A.; Schlattmann, R.; Unger, E.; Stegemann, B. Ablation mechanisms of nanosecond and picosecond laser scribing for metal halide perovskite module interconnection—An experimental and numerical analysis. *Sol. Energy* **2020**, *198*, 410–418. [[CrossRef](#)]
10. Li, J.; Dagar, J.; Shargaieva, O.; Flatken, M.A.; Köbler, H.; Fenske, M.; Schultz, C.; Stegemann, B.; Just, J.; Töbrens, D.M.; et al. 20.8% Slot-Die Coated MAPbI₃ Perovskite Solar Cells by Optimal DMSO-Content and Age of 2-ME Based Precursor Inks. *Adv. Energy Mater.* **2021**, *11*, 2003460. [[CrossRef](#)]
11. Dagar, J.; Castro-Hermosa, S.; Gasbarri, M.; Palma, A.L.; Cina, L.; Matteocci, F.; Calabrò, E.; Di Carlo, A.; Brown, T.M. Efficient fully laser-patterned flexible perovskite modules and solar cells based on low-temperature solution-processed SnO₂/mesoporous-TiO₂ electron transport layers. *Nano Res.* **2018**, *11*, 2669–2681. [[CrossRef](#)]
12. Palma, A.L.; Matteocci, F.; Agresti, A.; Pescetelli, S.; Calabrò, E.; Vesce, L.; Christiansen, S.; Schmidt, M.; Di Carlo, A. Laser-Patterning Engineering for Perovskite Solar Modules with 95% Aperture Ratio. *IEEE J. Photovolta.* **2017**, *7*, 1674–1680. [[CrossRef](#)]
13. Calabrò, E.; Matteocci, F.; Palma, A.L.; Vesce, L.; Taheri, B.; Carlini, L.; Pis, I.; Nappini, S.; Dagar, J.; Battocchio, C.; et al. Low temperature, solution-processed perovskite solar cells and modules with an aperture area efficiency of 11%. *Sol. Energy Mater. Sol. Cells* **2018**, *185*, 136–144. [[CrossRef](#)]
14. Mincuzzi, G.; Palma, A.L.; Di Carlo, A.; Brown, T.M. Laser Processing in the Manufacture of Dye-Sensitized and Perovskite Solar Cell Technologies. *ChemElectroChem* **2015**, *3*, 9–30. [[CrossRef](#)]
15. Matteocci, F.; Vesce, L.; Kosasih, F.U.; Castriotta, L.A.; Cacovich, S.; Palma, A.L.; Divitini, G.; Ducati, C.; Di Carlo, A. Fabrication and Morphological Characterization of High-Efficiency Blade-Coated Perovskite Solar Modules. *ACS Appl. Mater. Interfaces* **2019**, *11*, 25195–25204. [[CrossRef](#)] [[PubMed](#)]
16. Fenske, M.; Schultz, C.; Dagar, J.; Kosasih, F.U.; Zeiser, A.; Junghans, C.; Bartelt, A.; Ducati, C.; Schlattmann, R.; Unger, E.; et al. Improved Electrical Performance of Perovskite Photovoltaic Mini-Modules through Controlled PbI₂ Formation Using Nanosecond Laser Pulses for P3 Patterning. *Energy Technol.* **2021**, *9*, 2000969. [[CrossRef](#)]
17. Heo, J.H.; Han, H.J.; Kim, D.; Ahn, T.K.; Im, S.H. Hysteresis-less inverted CH₃NH₃PbI₃ planar perovskite hybrid solar cells with 18.1% power conversion efficiency. *Energy Environ. Sci.* **2015**, *8*, 1602–1608. [[CrossRef](#)]
18. Al-Ashouri, A.; Köhnen, E.; Li, B.; Magomedov, A.; Hempel, H.; Caprioglio, P.; Márquez, J.A.; Vilches, A.B.M.; Kasparavicius, E.; Smith, J.A.; et al. Monolithic perovskite/silicon tandem solar cell with >29% efficiency by enhanced hole extraction. *Science* **2020**, *370*, 1300–1309. [[CrossRef](#)]
19. Al-Ashouri, A.; Magomedov, A.; Roß, M.; Jošt, M.; Talaikis, M.; Chistiakova, G.; Bertram, T.; Márquez, J.A.; Köhnen, E.; Kasparavičius, E.; et al. Conformal monolayer contacts with lossless interfaces for perovskite single junction and monolithic tandem solar cells. *Energy Environ. Sci.* **2019**, *12*, 3356–3369. [[CrossRef](#)]
20. Moon, S.-J.; Yum, J.-H.; Lofgren, L.; Walter, A.; Sansonnens, L.; Benkhaira, M.; Nicolay, S.; Bailat, J.; Ballif, C. Laser-Scribing Patterning for the Production of Organometallic Halide Perovskite Solar Modules. *IEEE J. Photovolta.* **2015**, *5*, 1087–1092. [[CrossRef](#)]
21. Rakocevic, L.; Mundt, L.E.; Gehlhaar, R.; Merckx, T.; Aernouts, T.; Schubert, M.C.; Glunz, S.W.; Poortmans, J. Loss Analysis in Perovskite Photovoltaic Modules. *Sol. RRL* **2019**, *3*, 1900338. [[CrossRef](#)]
22. Volkov, A. Structure and mechanical properties of CuAu and CuAuPd ordered alloys. *Gold Bull.* **2004**, *37*, 208–215. [[CrossRef](#)]
23. Xie, Y.-Q.; Li, Y.-F.; Liu, X.-B.; Li, X.-B.; Peng, H.-J.; Nie, Y.-Z. Characteristic atom occupation patterns of Au₃Cu, AuCu₃, AuCuI and AuCuII based on experimental data of disordered alloys. *Trans. Nonferr. Met. Soc. China* **2011**, *21*, 1092–1104. [[CrossRef](#)]
24. Jiang, Z.; Chen, X.; Lin, X.; Jia, X.; Wang, J.; Pan, L.; Huang, S.; Zhu, F.; Sun, Z. Amazing stable open-circuit voltage in perovskite solar cells using AgAl alloy electrode. *Sol. Energy Mater. Sol. Cells* **2016**, *146*, 35–43. [[CrossRef](#)]
25. Lai, W.-C.; Lin, K.-W.; Guo, T.-F.; Chen, P.; Liao, Y.-Y. Efficient CH₃NH₃PbI₃ perovskite/fullerene planar heterojunction hybrid solar cells with oxidized Ni/Au/Cu transparent electrode. *Appl. Phys. Lett.* **2018**, *112*, 71103. [[CrossRef](#)]
26. An, Z.; Li, J.; Kikuchi, A.; Wang, Z.; Jiang, Y.; Ono, T. Mechanically strengthened graphene-Cu composite with reduced thermal expansion towards interconnect applications. *Microsyst. Nanoeng.* **2019**, *5*, 20. [[CrossRef](#)] [[PubMed](#)]
27. Barngrover, B.M.; Aikens, C.M. Incremental Binding Energies of Gold(I) and Silver(I) Thiolate Clusters. *J. Phys. Chem. A* **2011**, *115*, 11818–11823. [[CrossRef](#)] [[PubMed](#)]
28. Unger, E.; Paramasivam, G.; Abate, A. Perovskite solar cell performance assessment. *J. Phys. Energy* **2020**, *2*, 044002. [[CrossRef](#)]
29. Khenkin, M.V.; Anoop, K.M.; Visoly-Fisher, I.; Galagan, Y.; Di Giacomo, F.; Patil, B.R.; Sherafatipour, G.; Turkovic, V.; Rubahn, H.-G.; Madsen, M.; et al. Reconsidering figures of merit for performance and stability of perovskite photovoltaics. *Energy Environ. Sci.* **2018**, *11*, 739–743. [[CrossRef](#)]
30. Terrestrial Photovoltaic (PV) Modules—Design Qualification and Type Approval—Part 1: Test Requirements. Available online: https://infostore.saiglobal.com/preview/258973459811.pdf?sku=880220_SAIG_NSAI_NSAI_2091247 (accessed on 19 December 2016).
31. Qian, J.; Ernst, M.; Wu, N.; Blakers, A. Impact of perovskite solar cell degradation on the lifetime energy yield and economic viability of perovskite/silicon tandem modules. *Sustain. Energy Fuels* **2019**, *3*, 1439–1447. [[CrossRef](#)]